Electronic Supplementary Information

How nanotextured interfaces influence the electronics in perovskite solar cells

Dilara Abdel,[1] Jacob Relle,[2,3] Thomas Kirchartz,[4,5] Patrick Jaap,[6] Jürgen Fuhrmann,[6] Sven Burger,[3,7] Christiane Becker,[2,8,a)] Klaus Jäger,[2,3,b)] and Patricio Farrell[1,c)]

[1)] *Numerical Methods for Innovative Semiconductor Devices, Weierstrass Institute for Applied Analysis and Stochastics (WIAS), Berlin, Germany*

[2)] *Dept. Optics for Solar Energy, Helmholtz-Zentrum Berlin für Materialien und Energie GmbH, Berlin, Germany*

[3)] *Computational Nano Optics, Zuse Institute Berlin, Berlin, Germany*

[4)] *IMD-3 Photovoltaics, Forschungszentrum Jülich GmbH, Jülich, Germany*

[5)] *University of Duisburg-Essen, Duisburg, Germany*

[6)] *Numerical Mathematics and Scientific Computing, Weierstrass Institute for Applied Analysis and Stochastics (WIAS), Berlin, Germany*

[7)] *JCMwave GmbH, Berlin, Germany*

[8)] *Hochschule für Technik und Wirtschaft Berlin, Berlin, Germany*

[a)] E-mail: christiane.becker@helmholtz-berlin.de

[b)] E-mail: klaus.jaeger@helmholtz-berlin.de

[c)] E-mail: patricio.farrell@wias-berlin.de

CONTENTS

S1. Optical model and simulation 2

A. Model description 3

B. Optical material properties 3

S2. Electronic model and simulation 3

A. Model description 4

B. Electronic material parameters 6

S3. Additional electronic results 8

A. Recombination currents 8

B. Carrier densities and electric field for low surface recombination 10

C. Carrier densities and electric field for reference configuration 12

S4. Optical convergence scan 14

References 16

This *Electronic Supplementary Information* (ESI) provides additional insights into the opto-electronic properties of nanotextured perovskite solar cells. In Sections S1 and S2, we provide further details on the optical and electronic models, as well as the simulation methodology. All relevant material parameters used in this study are listed. Section S3 presents additional simulation results, including charge carrier densities and electric fields. Finally, Section S4 provides a convergence scan for the photogeneration profile and the calculated maximal achievable short circuit current density.

S1. OPTICAL MODEL AND SIMULATION

We model the interaction of the electromagnetic radiation from the Sun with the solar cell by using a time-harmonic formulation of the Maxwell equations, applied to the setup shown in Fig. **??**b. The problem is discretised via the finite element method (FEM), as implemented in the software `JCMsuite`.[1] This method uses a finite dimensional function space to solve a weak version of Maxwell's equations on a discretised mesh.

A. Model description

The optical model is based on the time-harmonic Maxwell equations, with the electric field $\mathbf{E}$ as the primary unknown:

$$\nabla \times \mu^{-1} \nabla \times \mathbf{E} - \omega^2 \epsilon \mathbf{E} = i\omega \mathbf{j}^{\mathrm{imp}}, \tag{S1.1}$$

where μ is the magnetic permeability μ, $\epsilon = \epsilon_0 \epsilon_r$ is the complex electric permittivity, with ϵ_0 denoting the vacuum permittivity and ϵ_r the relative permittivity. The angular frequency ω is related to the vacuum wavelength λ by $\omega = 2\pi c/\lambda$, and $\mathbf{j}^{\mathrm{imp}}$ denotes the impressed current density.[2]

We assume transparent boundary conditions on top and bottom of the device, which we implement via perfectly matched layers (PML). Bloch-periodic boundary conditions are applied in horizontal directions.[1] The source term is modelled by a plane wave solution in the exterior domain

$$\mathbf{E} = \mathbf{E}_0 \exp(i\mathbf{k}\mathbf{x}), \tag{S1.2}$$

where the wave vector $\mathbf{k}$ and the field amplitude $\mathbf{E}_0$ are determined by the angle of incidence ϕ and the polarization of the wave. In our simulations, the wave enters at normal incidence from the top of the device, i.e., $\phi = 0$. Therefore, the usual *sp*-polarization is expressed via polarization in either the x- or z-direction. To account for the unpolarised nature of sunlight, each wavelength is modelled twice: once with x-polarisation and once with z-polarization. The results are then averaged, assuming that both polarizations contribute equally to the total power. For simplicity, the total incoming power is normalised for each wavelength. The resulting optical response is then rescaled according to the corresponding irradiance Φ_e of the AM1.5G solar reference spectrum. The spectral irradiance Φ_e follows the ASTM G-173-03 standard,[3] provided by the U.S. Department of Energy (DOE)/NREL/ALLIANCE. Additional details on the modelling approach can be found in the solver documentation.[1]

B. Optical material properties

Wavelength-dependent complex refractive index data $n + ik$ are given for all materials in the relevant wavelength range of the solar spectrum. To interpolate the data and calculate $\epsilon_r = (n + ik)^2$ for the desired wavelengths, we use the Python package `dispersion`.[4] The underlying n, k datasets were taken from various literature sources, which are summarized in Tab. S1.

S2. ELECTRONIC MODEL AND SIMULATION

We model the charge transport using a vacancy-assisted drift-diffusion model within a three-layer solar setup as shown in Fig. **??**a. For clarity, we denote the total three-layer device geometry by Ω, the electron

TABLE S1. Used materials, their thickness in the simulation and references of the used n, k datasets. *For the perovskite layer (PVK), the thickness denotes the *effective thickness*, i.e., the thickness of a planar layer with the same volume.

Material	Thickness	Source of n, k dataset
Glass	1000 nm	Delivered with `GenPro4`[5]
ITO	135 nm	L. Mazzarella *et al.*[6]
PTAA	10 nm	Delivered with `GenPro4`[5]
PVK	400 nm*	J.A. Guerra *et al.*[7]
C_{60}	30 nm	D. Menzel *et al.*[8]
Cu	100 nm	P.B. Johnson and R.W. Christy[8]

transport layer (ETL) by Ω_{ETL}, the intrinsic perovskite absorber (PVK) layer by Ω_{PVK}, and the hole transport layer (HTL) by Ω_{HTL}. Electrons and holes are allowed to migrate throughout the entire device. In contrast, vacancy migration is restricted to the perovskite layer Ω_{PVK}, where we account for volume exclusion effects. The system is discretized using an implicit-in-time finite volume scheme, which ensures local flux conservation and consistency with thermodynamic laws – key advantages of the finite volume method (FVM). Moreover, the existence and boundedness of both weak and discrete FVM solutions have been rigorously established.[9,10] For a detailed discussion of the model and the discretization, we refer to previous studies.[11–13]

A. Model description

Charge transport equations The charge transport model considers the electric potential ψ and the quasi Fermi potentials of moving charge carriers φ_α as unknowns. Here, the indices $\alpha \in \{\mathrm{n}, \mathrm{p}, \mathrm{a}\}$ refer to the electrons, holes, and anion vacancies. Within the perovskite layer Ω_{PVK}, carrier transport is governed by the following equations

$$-\nabla \cdot (\varepsilon_s \nabla \psi) = q\Big(z_{\mathrm{n}} n_{\mathrm{n}} + z_{\mathrm{p}} n_{\mathrm{p}} + z_{\mathrm{a}} n_{\mathrm{a}} + C(\mathbf{x})\Big), \tag{S2.1a}$$

$$z_{\mathrm{n}} q \partial_t n_{\mathrm{n}} + \nabla \cdot \mathbf{j}_{\mathrm{n}} = z_{\mathrm{n}} q \left(G(\mathbf{x}) - R(n_{\mathrm{n}}, n_{\mathrm{p}})\right), \tag{S2.1b}$$

$$z_{\mathrm{p}} q \partial_t n_{\mathrm{p}} + \nabla \cdot \mathbf{j}_{\mathrm{p}} = z_{\mathrm{p}} q \left(G(\mathbf{x}) - R(n_{\mathrm{n}}, n_{\mathrm{p}})\right), \tag{S2.1c}$$

$$z_{\mathrm{a}} q \partial_t n_{\mathrm{a}} + \nabla \cdot \mathbf{j}_{\mathrm{a}} = 0. \tag{S2.1d}$$

Only electrons and holes are considered in the transport layers $\Omega_{\mathrm{ETL}} \cup \Omega_{\mathrm{HTL}}$, meaning the model reduces to equations (S2.1a)-(S2.1c) with a modified space charge density in that case. The dielectric permittivity is defined as $\varepsilon_s = \varepsilon_0 \varepsilon_r$, where ε_0 is the vacuum permittivity and ε_r the relative material permittivity.

The charge numbers are given by $z_\mathrm{n} = -1$, $z_\mathrm{p} = 1$, and $z_\mathrm{a} = 1$. The doping and the mean vacancy concentration are included in the quantity C. Moreover, G denotes the optical photogeneration rate and R the recombination processes. Finally, the current density $\mathbf{j}_\alpha$ describes the motion of charge carriers

$$\mathbf{j}_\alpha = -z_\alpha q \left(D_\alpha \left(\frac{n_\alpha}{N_\alpha} \right) \nabla n_\alpha + z_\alpha \mu_\alpha n_\alpha \nabla \psi \right), \quad \alpha \in \{\mathrm{n}, \mathrm{p}, \mathrm{a}\}, \tag{S2.2}$$

where D_α represents the non-linear diffusion coefficient and μ_α the mobility of carriers. We can link the charge carrier densities n_α to the potentials, defining the set of unknowns, for $\alpha \in \{\mathrm{n}, \mathrm{p}, \mathrm{a}\}$ via

$$n_\alpha = N_\alpha \mathcal{F}_\alpha\Big(\eta_\alpha(\varphi_\alpha, \psi)\Big), \quad \eta_\alpha = \frac{\Phi_\alpha}{k_B T} = \frac{z_\alpha \left(E_\alpha - E_{\mathrm{F},\alpha}\right)}{k_B T} = z_\alpha \frac{q(\varphi_\alpha - \psi) + E_{\alpha,0}}{k_B T}. \tag{S2.3}$$

Here, T is the temperature, k_B is the Boltzmann constant, and $N_\mathrm{c} = N_\mathrm{n}$ and $N_\mathrm{v} = N_\mathrm{p}$ are the effective densities of state of the conduction band and valence band. The parameters $E_{\mathrm{c},0} = E_{\mathrm{n},0}$ and $E_{\mathrm{v},0} = E_{\mathrm{p},0}$ denote the intrinsic band edge energies of the conduction and valence bands for electrons and holes. In contrast, $E_{\mathrm{a},0}$ corresponds to an intrinsic energy level of vacancies. The quantities $\Phi_\mathrm{n} = z_\mathrm{n}(E_\mathrm{c} - E_{\mathrm{F,n}})$ and $\Phi_\mathrm{p} = z_\mathrm{p}(E_\mathrm{v} - E_{\mathrm{F,p}})$ are the energy off-sets of electrons and holes, respectively. Moreover, $E_{\mathrm{F,\,n}} = -q\varphi_\mathrm{n}$ is the electron quasi Fermi level and $E_{\mathrm{F,\,p}} = -q\varphi_\mathrm{p}$ is the hole quasi Fermi level. The statistics function $\mathcal{F}_\alpha$ varies depending on the type of charge carrier. For electrons and holes, $\mathcal{F}_\mathrm{n}$ and $\mathcal{F}_\mathrm{p}$ depend on the semiconductor material: the Fermi-Dirac integral of order $1/2$ is used for inorganic materials, while organic materials require the Gauss-Fermi integral. In the limit of $n_\alpha \ll N_\alpha$ both integrals are well approximated by $\mathcal{F}_\mathrm{n} = \mathcal{F}_\mathrm{p} \approx \exp$ which is the case here. In contrast, for vacancies the function $\mathcal{F}_\alpha(\eta) = 1/(\exp(-\eta) + 1)$, called Fermi-Dirac integral of order -1, ensures the correct limitation of ion depletion. In (S2.3), N_a denotes a saturation density, limited by the density of available lattice sites in the crystal.

Recombination and photogeneration The recombination rate R on the right-hand side of the electron and hole mass balance equations (S2.1b)-(S2.1c) is modelled by the sum of the dominant recombination processes: Shockley-Read-Hall (SRH), radiative, and surface recombination with

$$R(n_\mathrm{n}, n_\mathrm{p}) = \sum_r R_r(n_\mathrm{n}, n_\mathrm{p}), \quad r \in \{\mathrm{SRH}, \mathrm{rad}, \mathrm{surf}\}. \tag{S2.4}$$

Each recombination contribution R_r follows the general form

$$R_r(n_\mathrm{n}, n_\mathrm{p}) = r_r(n_\mathrm{n}, n_\mathrm{p}) n_\mathrm{n} n_\mathrm{p} \left(1 - \exp\left(\frac{q\varphi_\mathrm{n} - q\varphi_\mathrm{p}}{k_B T}\right)\right). \tag{S2.5}$$

The process-dependent, non-negative rate functions r_r are defined as follows. First, for SRH recombination, we have

$$r_{\mathrm{SRH}}(n_\mathrm{n}, n_\mathrm{p}) = \frac{1}{\tau_\mathrm{p}(n_\mathrm{n} + n_{\mathrm{n},\tau}) + \tau_\mathrm{n}(n_\mathrm{p} + n_{\mathrm{p},\tau})}, \tag{S2.6}$$

where $\tau_\mathrm{n}, \tau_\mathrm{p}$ are the carrier lifetimes and $n_{\mathrm{n},\tau}, n_{\mathrm{p},\tau}$ are reference carrier densities. The SRH model assumes a single mid-gap trap level, consistent with prior work and the literature.[14–16] While more detailed models

that incorporate multiple defect levels exist, these are beyond the scope of the present study. Second, for the radiative recombination the prefactor is given by

$$r_{\mathrm{rad}}(n_{\mathrm{n}}, n_{\mathrm{p}}) = r_{0,\mathrm{rad}} \tag{S2.7}$$

for a constant rate coefficient $r_{0,\mathrm{rad}}$. Lastly, the surface recombination can be modelled as

$$r_{\mathrm{surf}}(n_{\mathrm{n}}, n_{\mathrm{p}}) = \frac{1}{\frac{1}{\nu_{\mathrm{p}}}(n_{\mathrm{n}} + n_{\mathrm{n},\tau}) + \frac{1}{\nu_{\mathrm{n}}}(n_{\mathrm{p}} + n_{\mathrm{p},\tau})}, \tag{S2.8}$$

where ν_{n}, ν_{p} are the surface recombination velocities. Unless stated otherwise, the photogeneration G, defined in the accompanying paper, is obtained as the solution of the time-harmonic Maxwell equations described in Section S1.

Boundary and initial conditions Following the device geometry depicted in Fig. **??**a, we assume that at the top and the bottom of the architecture, we have the metal-semiconductor interfaces, denoted by Γ^{D}. The left and right boundaries are denoted by Γ^{N}. We model the boundary conditions for $t \geq 0$ as follows:

$$\psi(\mathbf{x}, t) = \psi_0(\mathbf{x}) + V(\mathbf{x}, t), \;\; \varphi_{\mathrm{n}}(\mathbf{x}, t) = \varphi_{\mathrm{p}}(\mathbf{x}, t) = V(\mathbf{x}, t), \qquad \mathbf{x} \in \Gamma^{\mathrm{D}}, \tag{S2.9}$$

$$\nabla\psi(\mathbf{x}, t) \cdot \boldsymbol{\nu}(\mathbf{x}) = \mathbf{j}_{\mathrm{n}}(\mathbf{x}, t) \cdot \boldsymbol{\nu}(\mathbf{x}) = \mathbf{j}_{\mathrm{p}}(\mathbf{x}, t) \cdot \boldsymbol{\nu}(\mathbf{x}) = 0, \qquad \mathbf{x} \in \Gamma^{\mathrm{N}}. \tag{S2.10}$$

Here, V corresponds to the externally applied measurement protocol, and $\boldsymbol{\nu}$ denotes the outward pointing unit normal vector to Γ^{N}. The potential ψ_0, often referred to as built-in potential, will be specified in Section S2 B. Regarding the anion vacancies, we impose no flux Neumann boundary conditions on the entire boundary of the intrinsic layer, namely

$$\mathbf{j}_{\mathrm{a}}(\mathbf{x}, t) \cdot \boldsymbol{\nu}_{\mathrm{PVK}}(\mathbf{x}) = 0, \quad \mathbf{x} \in \partial\Omega_{\mathrm{PVK}}, \; t \geq 0, \tag{S2.11}$$

where $\boldsymbol{\nu}_{\mathrm{PVK}}$ is the outward pointing unit normal vector to $\partial\Omega_{\mathrm{PVK}}$.

Lastly, we supply the system with initial conditions for $t = 0$

$$\varphi_{\mathrm{n}}(\mathbf{x}, 0) = \varphi_{\mathrm{n}}^0(\mathbf{x}), \qquad \varphi_{\mathrm{p}}(\mathbf{x}, 0) = \varphi_{\mathrm{p}}^0(\mathbf{x}), \quad \mathbf{x} \in \Omega, \tag{S2.12a}$$

$$\varphi_{\mathrm{a}}(\mathbf{x}, 0) = \varphi_{\mathrm{a}}^0(\mathbf{x}), \qquad \mathbf{x} \in \Omega_{\mathrm{PVK}}. \tag{S2.12b}$$

The total current is obtained by integrating the sum of current densities over the device contacts, as determined from the numerical solution of the coupled system of partial differential equations.[17]

B. Electronic material parameters

Table S2 summarizes the electronic parameters used in all electronic simulations. In consistency with Thiesbrummel *et al.*,[18] we set the boundary values for the built-in potential as follows: at the bottom

contact, $\psi_0 = -(0.05\,\mathrm{eV} - E_{\mathrm{c},0})/q$, and at the top contact, $\psi_0 = -(-0.05\,\mathrm{eV} - E_{\mathrm{v},0})/q$, thereby including the energy offset 0.05 eV between the metal and the transport layer. Note that the scan protocol is applied at the top contact. Furthermore, we set the doping term on the right-hand side of the Poisson equation (S2.1a) to $C = C_{\mathrm{n}}$ in the electron transport layer, $C = -C_{\mathrm{a}}$ in the intrinsic perovskite layer and $C = -C_{\mathrm{p}}$ in the hole transport layer.

TABLE S2. Parameter values for the simulation of a single-junction "83-17 triple cation" perovskite solar cell at a temperature $T = 300\,\mathrm{K}$ with C_{60} as electron transport layer material and PTAA as hole transport layer material, mainly based on Thiesbrummel *et al.*,[18] for which a data publication is available. *For the perovskite layer, the thickness denotes the *effective thickness*, i.e., the thickness of a planar layer with the same volume.

Physical quantity	**Symbol**	**Value**			**Unit**	**Ref.**
		C_{60}	Perovskite	PTAA		
Layer thickness		30	400*	10	nm	14,18
Relative permittivity	ε_r	5	22.0	3.5		14,18
Conduction band-edge energy	$E_{\mathrm{c},0}$	−3.9	−3.9	−2.5	eV	14,18
Valence band-edge energy	$E_{\mathrm{v},0}$	−5.9	−5.53	−5.5	eV	14,18
Eff. conduction band DoS	N_{c}	1×10^{26}	2.2×10^{24}	1×10^{26}	m^{-3}	14,18
Eff. valence band DoS	N_{v}	1×10^{26}	2.2×10^{24}	1×10^{26}	m^{-3}	14,18
Max. vacancy density	N_{a}	–	1.0×10^{27}	–	m^{-3}	
Doping density	C_{n}	1.0×10^{20}	0.0	0.0	m^{-3}	
Doping density	C_{p}	0.0	0.0	1.0×10^{20}	m^{-3}	
Average vacancy density	C_{a}	–	6.0×10^{22}	–	m^{-3}	14
Electron mobility	μ_{n}	1.0×10^{-6}	1.0×10^{-4}	1.0×10^{-8}	$\mathrm{m}^2 \cdot (\mathrm{V\,s})^{-1}$	18
Hole mobility	μ_{p}	1.0×10^{-6}	1.0×10^{-4}	1.0×10^{-8}	$\mathrm{m}^2 \cdot (\mathrm{V\,s})^{-1}$	18
Vacancy mobility	μ_{a}	–	1.9×10^{-12}	–	$\mathrm{m}^2 \cdot (\mathrm{V\,s})^{-1}$	14
Rad. recombination coeff.	$r_{0,\mathrm{rad}}$	0.0	3.0×10^{-17}	0.0	$\mathrm{m}^3 \cdot \mathrm{s}^{-1}$	15,18
SRH lifetime, electrons	τ_{n}	1.0×10^{100}	2.0×10^{-7}	1.0×10^{100}	s	18,19
SRH lifetime, holes	τ_{p}	1.0×10^{100}	2.0×10^{-7}	1.0×10^{100}	s	18,19
SRH ref. dens. electrons	$n_{\mathrm{n},\tau}$	1.59×10^{9}	4.48×10^{10}	6.33	m^{-3}	
SRH ref. dens. holes	$n_{\mathrm{p},\tau}$	1.59×10^{9}	4.48×10^{10}	6.33	m^{-3}	

The surface recombination velocities at the perovskite/HTL interface v_{HTL} and at the ETL/PVK

interface are varied throughout our study. For the reference configuration,[18] we set $v_{\mathrm{HTL}} = v_{\mathrm{n}} = v_{\mathrm{p}} = 2000\,\mathrm{cm{\cdot}s^{-1}}$ and $v_{\mathrm{ETL}} = v_{\mathrm{n}} = v_{\mathrm{p}} = 500\,\mathrm{cm{\cdot}s^{-1}}$. To remain consistent with the literature,[14,18] we adopt the default SRH reference densities from the simulation tool `Ionmonger`,[16] which was used in the aforementioned studies.

Specifically, the reference densities in the surface recombination terms at the HTL/perovskite interface are set to $n_{\mathrm{n},\tau} = n_{\mathrm{n},\tau}|_{\Omega_{\mathrm{PVK}}}$ and $n_{\mathrm{p},\tau} = n_{\mathrm{p},\tau}|_{\Omega_{\mathrm{HTL}}}$, while at the perovskite/ETL interface we have $n_{\mathrm{n},\tau} = n_{\mathrm{n},\tau}|_{\Omega_{\mathrm{ETL}}}$ and $n_{\mathrm{p},\tau} = n_{\mathrm{p},\tau}|_{\Omega_{\mathrm{PVK}}}$, which are stated in Tab. S2.

In Thiesbrummel *et al.*,[18] the transport layers (TLs) are assumed to be undoped. For numerical stability, the doping in the TLs is set to $1.0 \times 10^{20}\,\mathrm{m^{-3}}$, which is small compared to the effective density of states for electrons and holes and can therefore be interpreted as effectively undoped. The maximum vacancy density N_{a} corresponds to a saturation limit that reflects the finite number of available lattice sites in the perovskite and can be estimated from the lattice constant.[13]

We note that for the one-dimensional planar setup, our simulations with `ChargeTransport.jl` match those obtained with `Ionmonger`, the simulation tool used in the aforementioned works.[14,15,18]

S3. ADDITIONAL ELECTRONIC RESULTS

In this section, we present additional figures that support the arguments made in the main text. Section S3 A provides the recombination current densities and Sections S3 B and S3 C show additional results for the low-surface-recombination case (C_4) and the reference configuration (C_1), respectively. For the intermediate test cases C_2 and C_3 we have similar results.

A. Recombination currents

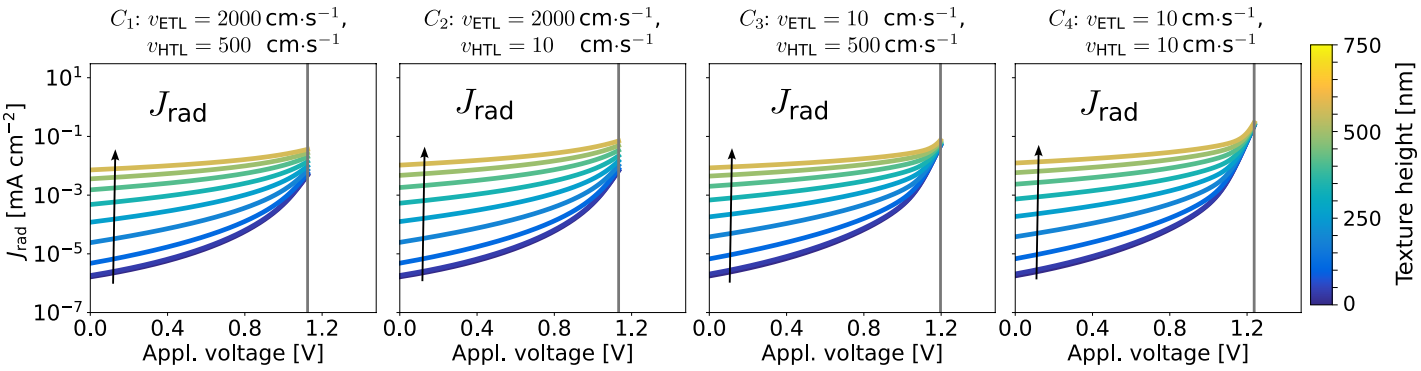

FIG. S1. Radiative recombination current density J_{rad} for all four test cases C_1 to C_4 for varying texture heights. The arrows indicate the direction of increasing texture height.

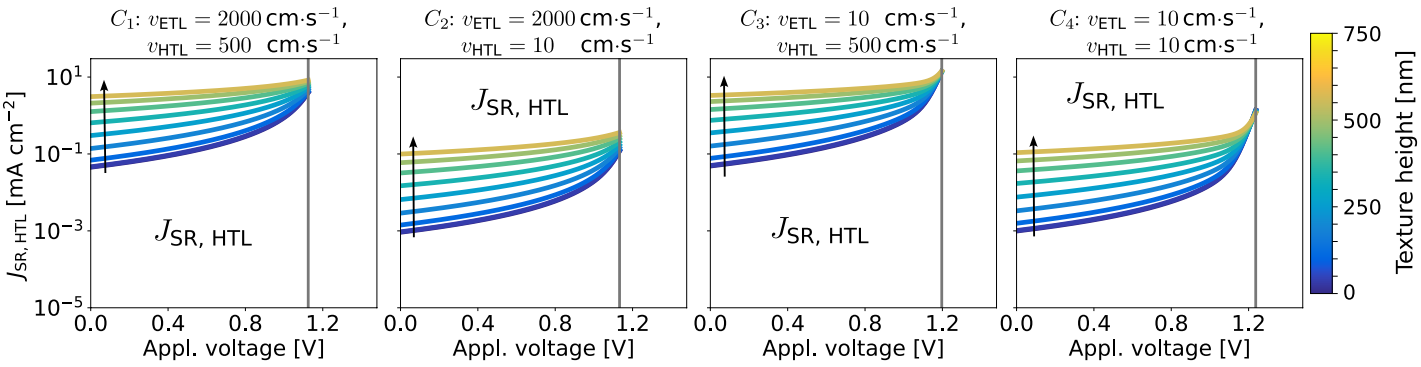

FIG. S2. Surface recombination current density at the PVK/HTL interface $J_{\mathrm{SR,\,HTL}}$ for all four test cases C_1 to C_4 for varying texture heights. The arrows indicate the direction of increasing texture height.

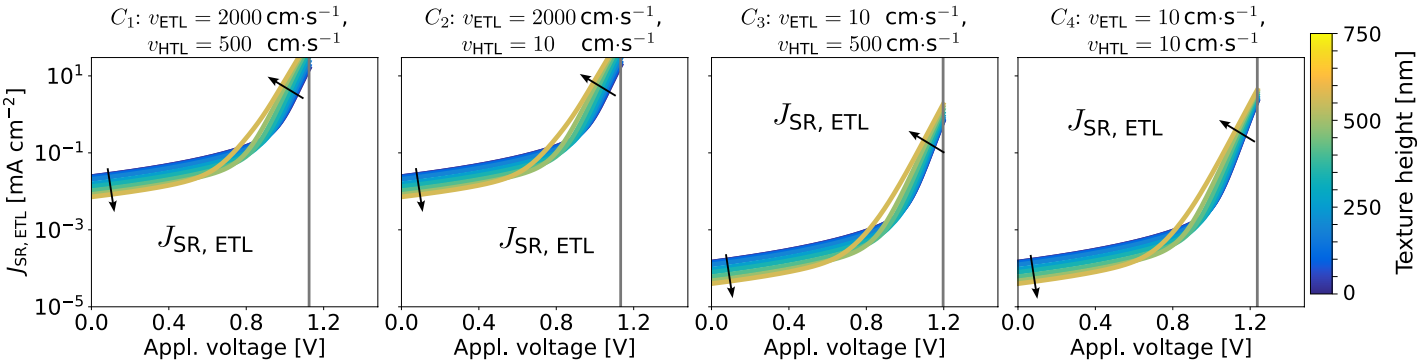

FIG. S3. Surface recombination current density at the ETL/PVK interface $J_{\mathrm{SR,\,ETL}}$ for all four test cases C_1 to C_4 for varying texture heights. The arrows indicate the direction of increasing texture height.

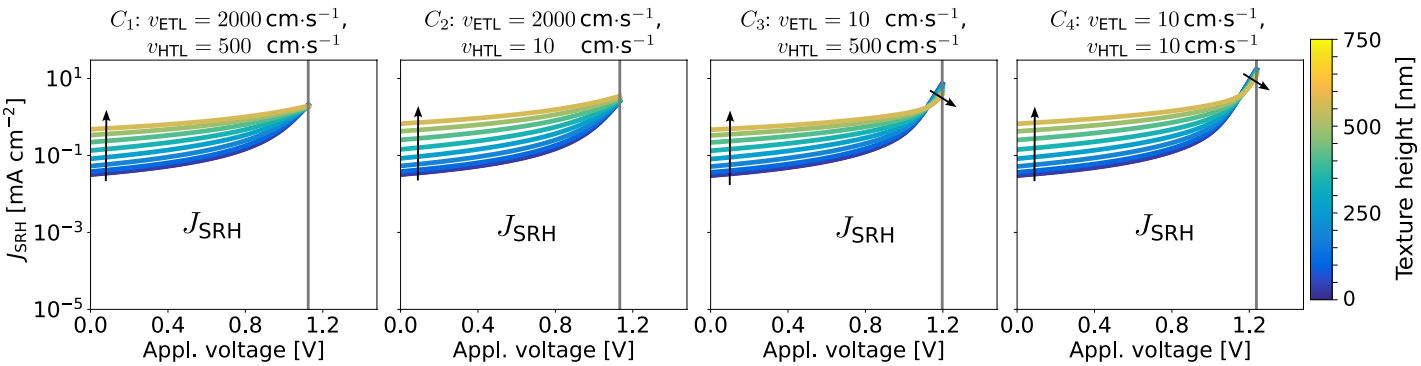

FIG. S4. Shockley-Read-Hall recombination current density J_{SRH} for all four test cases C_1 to C_4 for varying texture heights. The arrows indicate the direction of increasing texture height.

B. Carrier densities and electric field for low surface recombination

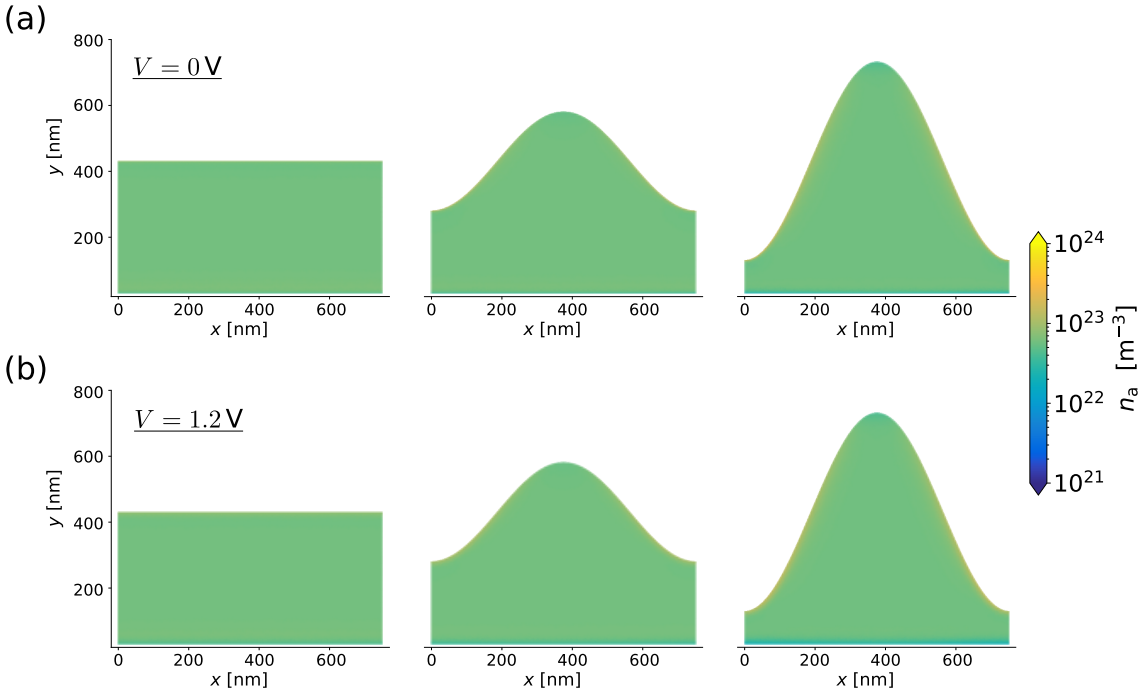

FIG. S5. Simulated vacancy density n_a within the PVK layer for the studied solar cell setup during the forward scan for the test case C_4 at (a) zero applied voltage and (b) an applied voltage near open-circuit voltage ($V = 1.2\,\mathrm{V}$). We have an average vacancy density of $\overline{n_\mathrm{a}} = 6.0 \times 10^{22}\,\mathrm{m}^{-3}$ for all texture heights.

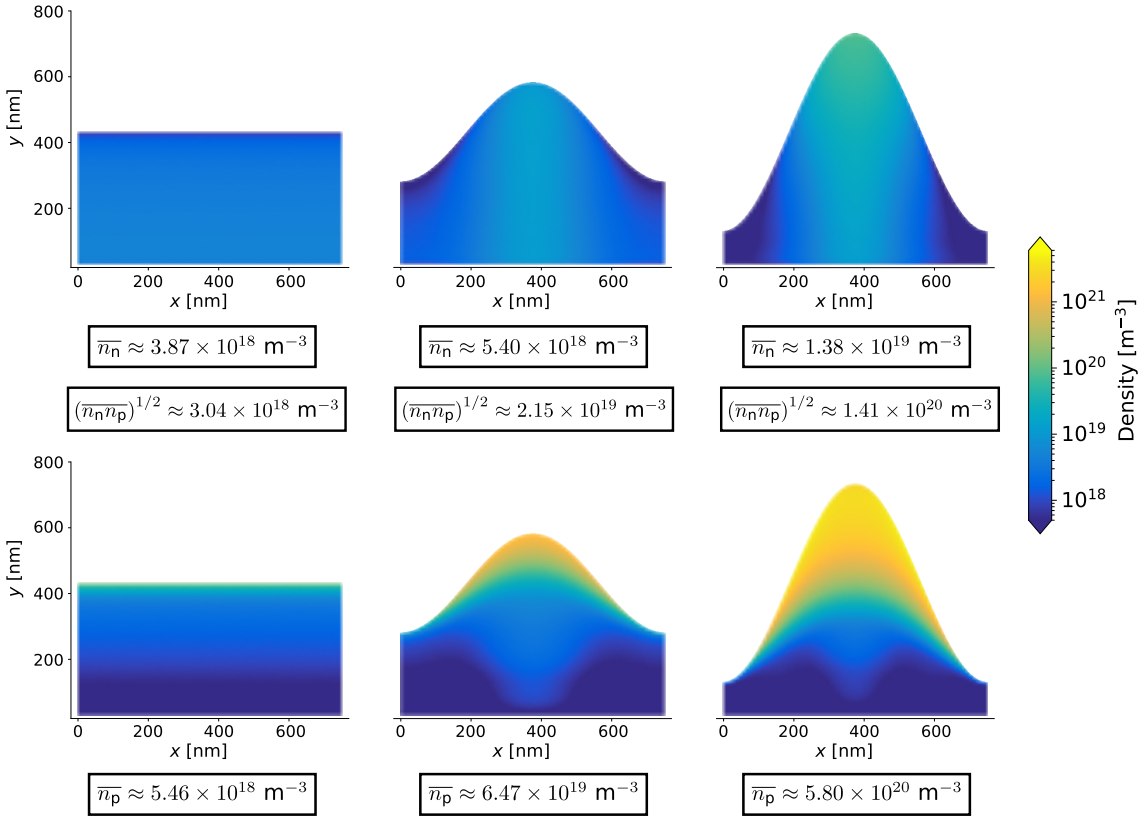

FIG. S6. Simulated charge carrier densities of electrons n_n and holes n_p during the forward scan for the test case C_4 at an applied voltage near short-circuit conditions ($V = 0\,\mathrm{V}$). The boxes indicate the integral averages of the densities over the perovskite material layer.

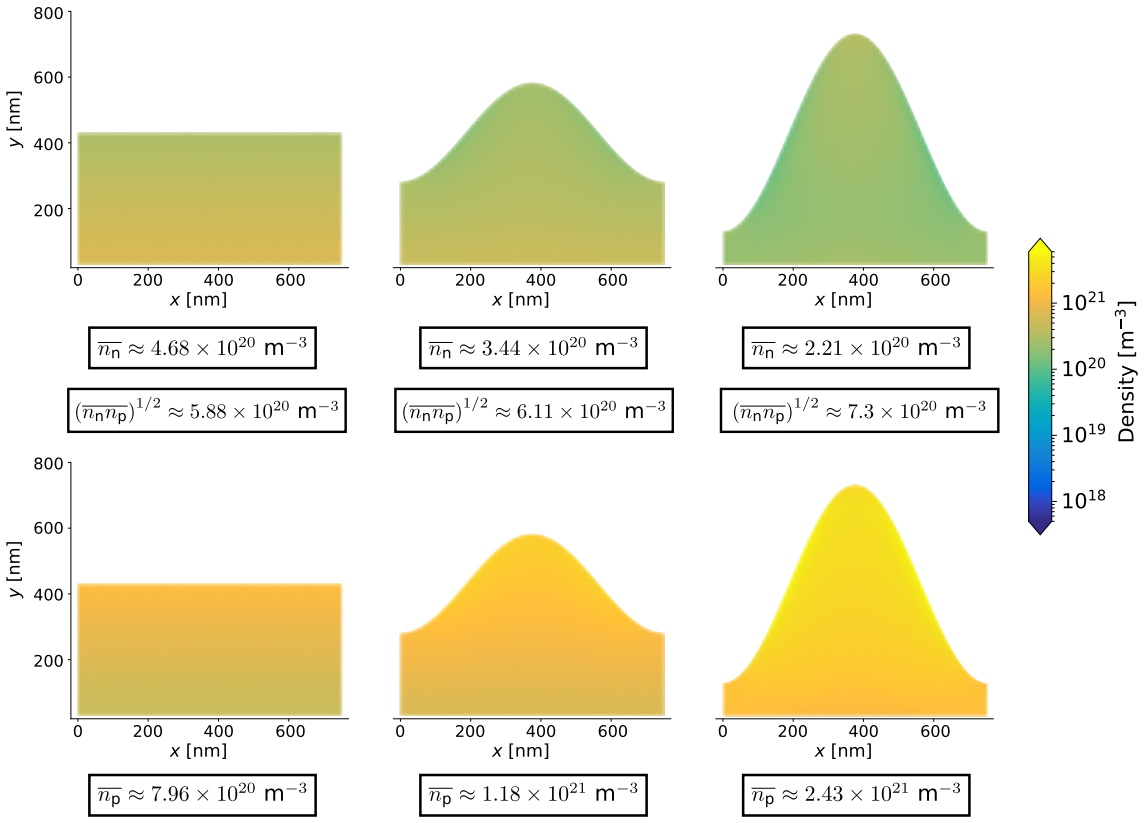

FIG. S7. Simulated charge carrier densities of electrons n_n and holes n_p during the forward scan for the test case C_4 at an applied voltage near open-circuit ($V = 1.2\,\mathrm{V}$). The boxes indicate the integral averages of the densities over the perovskite material layer.

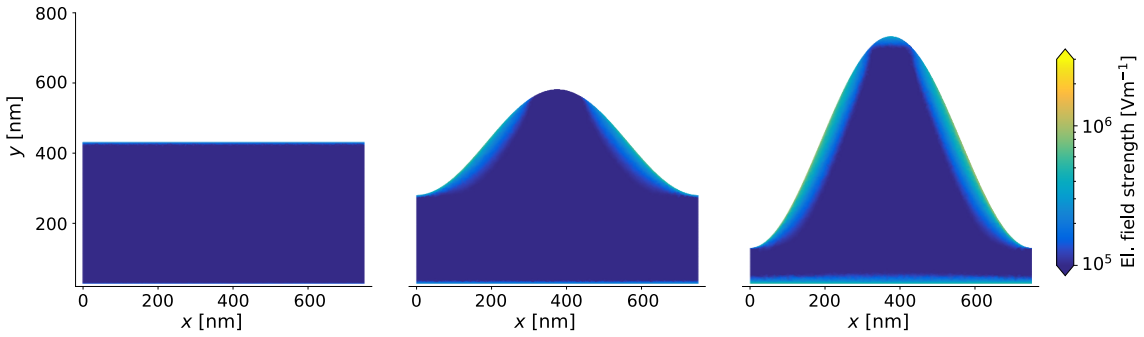

FIG. S8. Simulated electric field for the test case C_4 at an applied voltage near open-circuit ($V = 1.2\,\mathrm{V}$). The colour and the stream plot indicate the strength $\| -\nabla\psi\|_2$ and the direction of the electric field, respectively.

C. Carrier densities and electric field for reference configuration

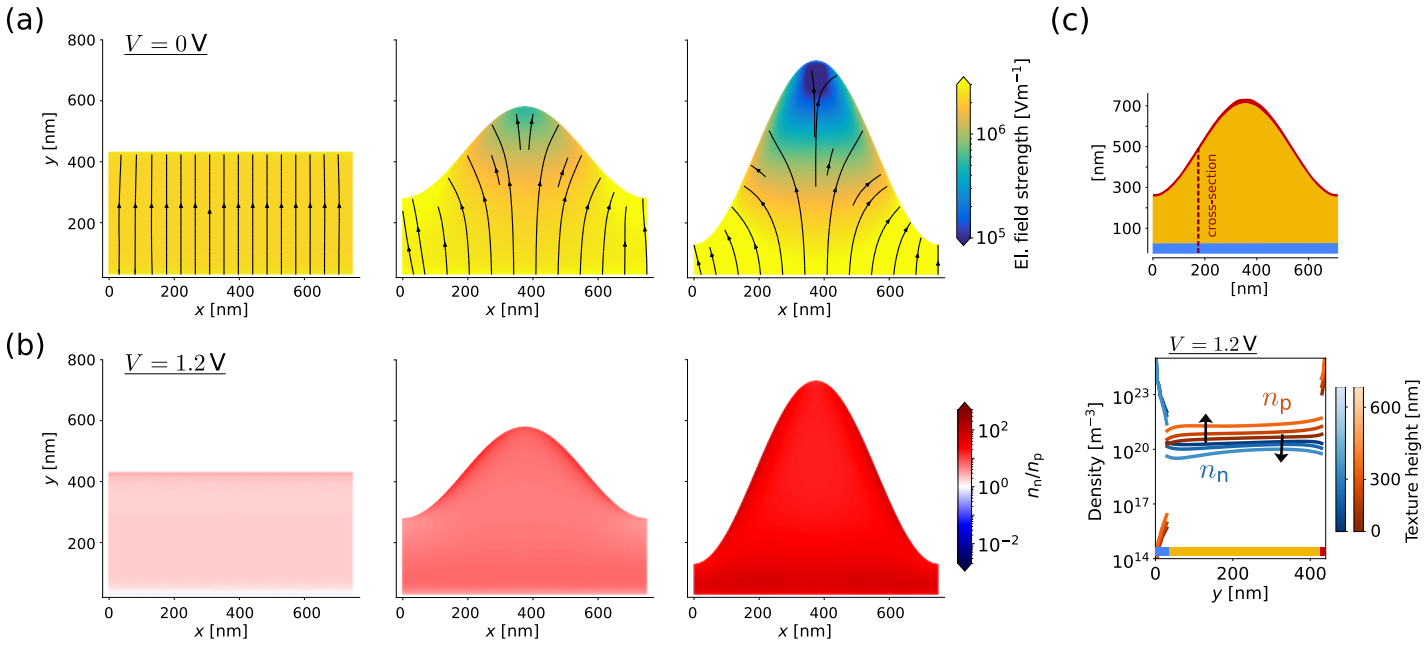

FIG. S9. Analogously to Fig. **??**, we show the electric field and carrier densities for the test case C_1 (reference configuration). (a) Electric field for three texture heights $h_T = 0, 300, 600\,\mathrm{nm}$ for $V = 0\,\mathrm{V}$ applied voltage. The colour and the stream plot indicate the strength $\| -\nabla\psi\|_2$ and the direction of the electric field, respectively. (b) The corresponding ratio between hole and electron density n_p/n_n for $V = 1.2\,\mathrm{V}$ applied voltage. (c) 2D device geometry with the vertical cross-section indicated (top), along which the carrier densities (bottom) are extracted. More precisely, we see one-dimensional profiles of the electron (blue) and hole densities (red) at an applied voltage $V = 1.2\,\mathrm{V}$ for varying texture height. In the density plot, brighter colours indicate greater texture height, with arrows showing the direction of increasing texture height.

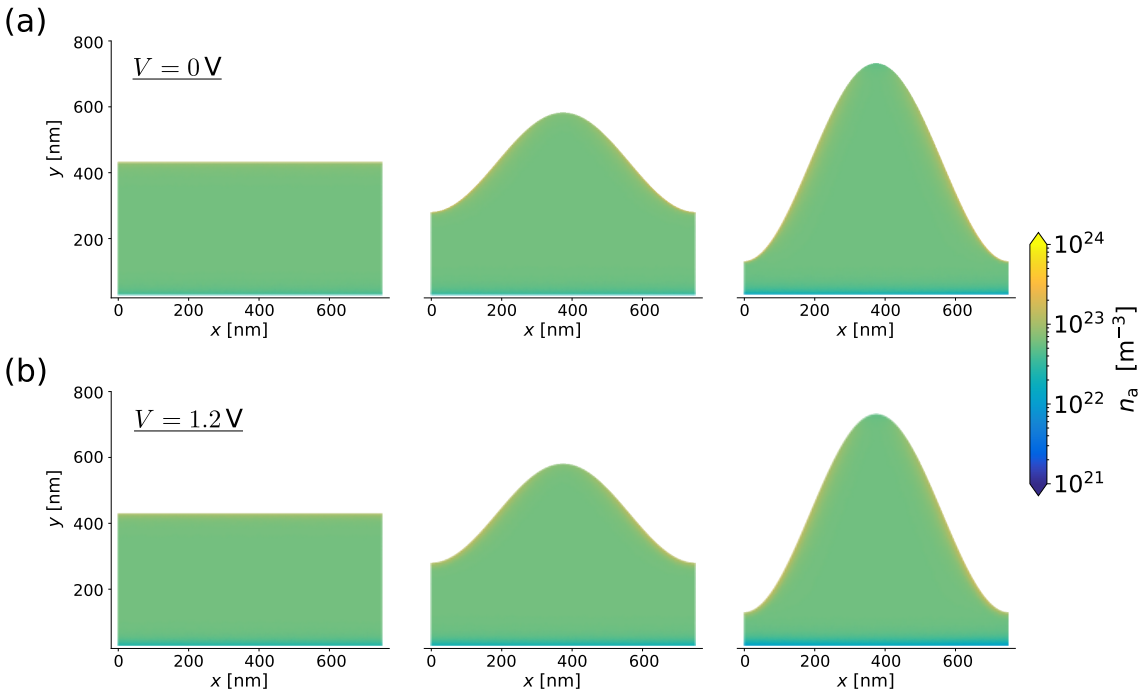

FIG. S10. Simulated vacancy density n_a within the PVK layer for the studied solar cell setup during the forward scan for the test case C_1 at (a) zero applied voltage and (b) an applied voltage near open-circuit voltage ($V = 1.2\,\mathrm{V}$). We have an average vacancy density of $\overline{n_\mathrm{a}} = 6.0 \times 10^{22}\,\mathrm{m}^{-3}$ for all texture heights.

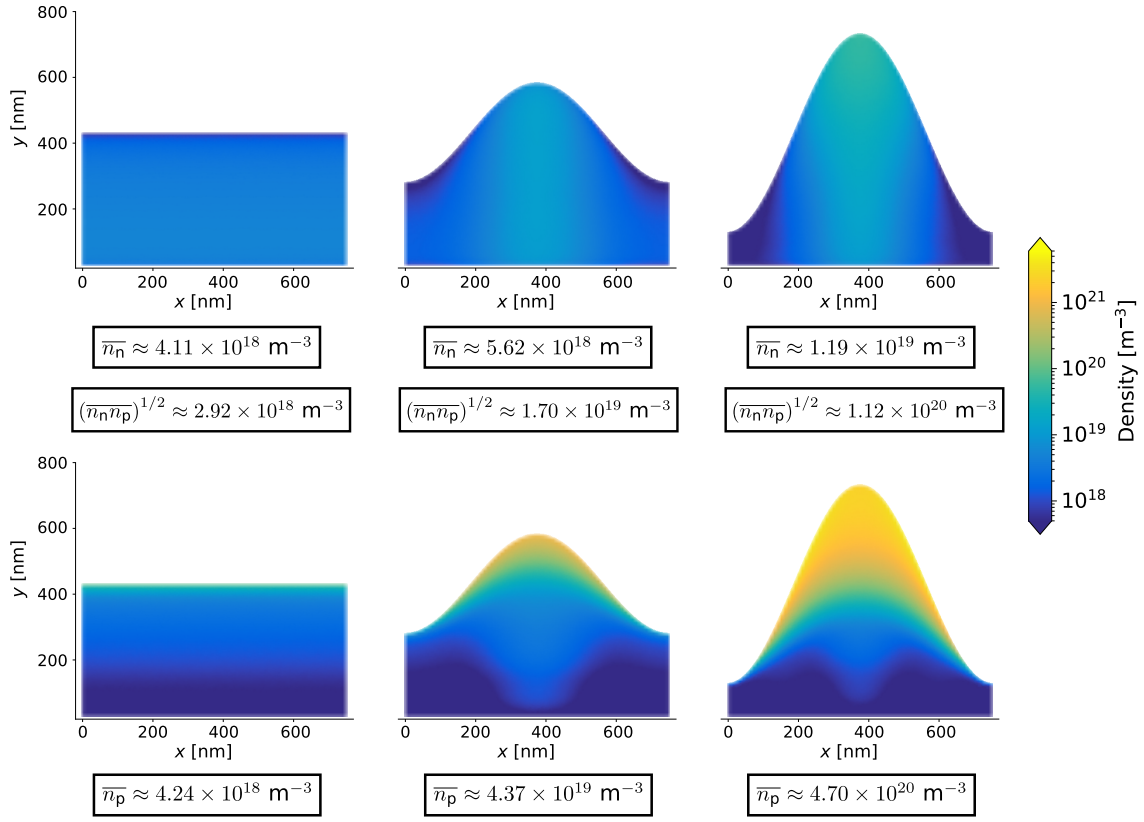

FIG. S11. Simulated charge carrier densities of electrons n_n and holes n_p during the forward scan for the test case C_1 at an applied voltage near short-circuit conditions ($V = 0\,\mathrm{V}$). The boxes indicate the integral averages of the densities over the perovskite material layer.

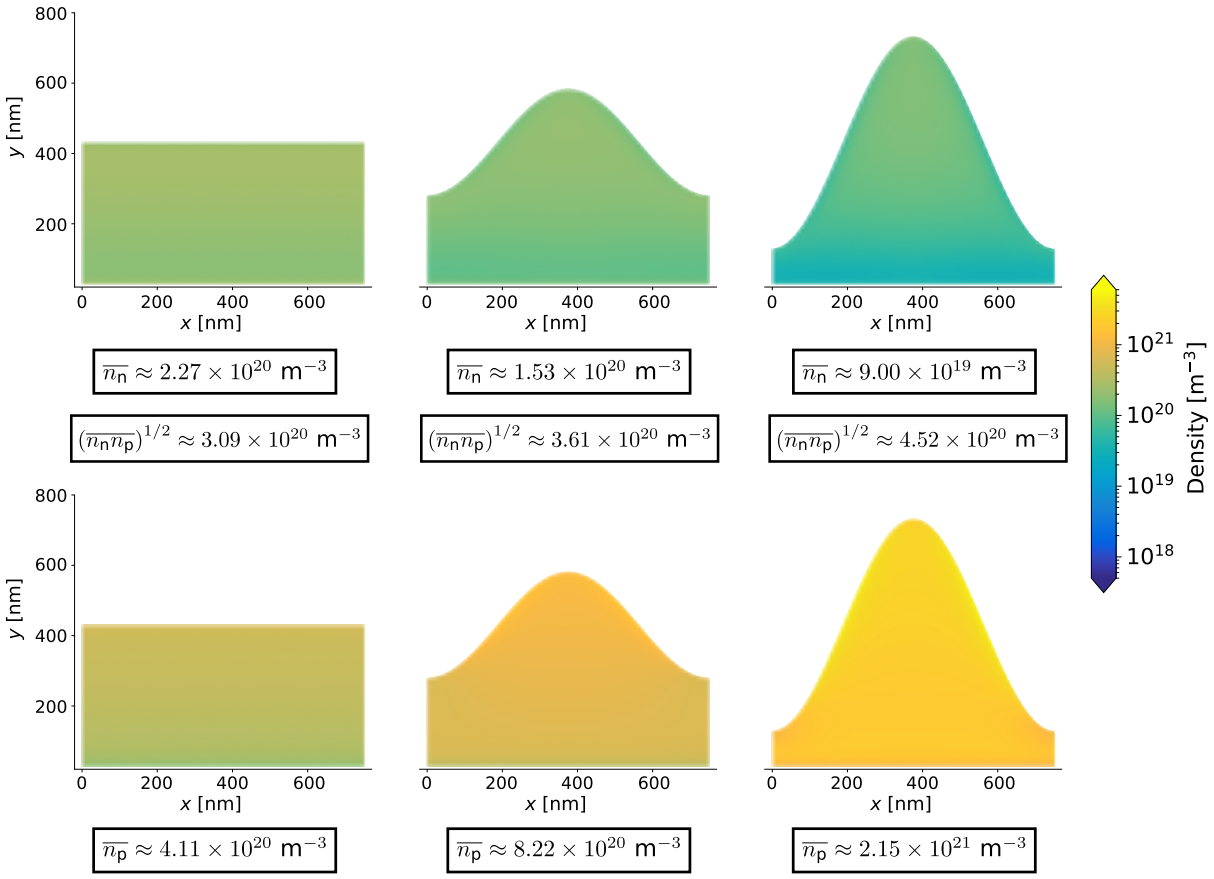

FIG. S12. Simulated charge carrier densities of electrons n_n and holes n_p during the forward scan for the test case C_1 at an applied voltage near open-circuit voltage ($V = 1.2\,\mathrm{V}$). The boxes indicate the integral averages of the densities over the perovskite material layer.

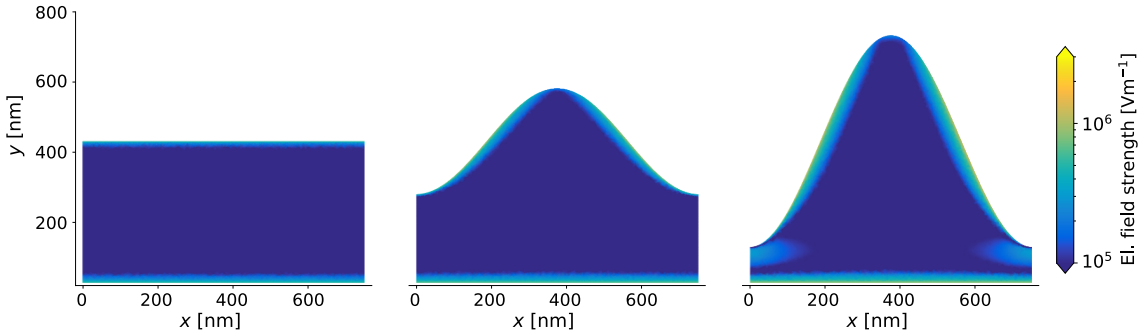

FIG. S13. Simulated electric field for the test case C_1 at an applied voltage near open-circuit ($V = 1.2\,\mathrm{V}$). The colour and the stream plot indicate the strength $\| -\nabla\psi\|_2$ and the direction of the electric field, respectively.

S4. OPTICAL CONVERGENCE SCAN

We check the convergence of the optical simulations.

The accuracy of the FEM simulations is primarily determined by two parameters: the polynomial degree p and the maximum element side length h. Higher polynomial degrees p improve the approxi-

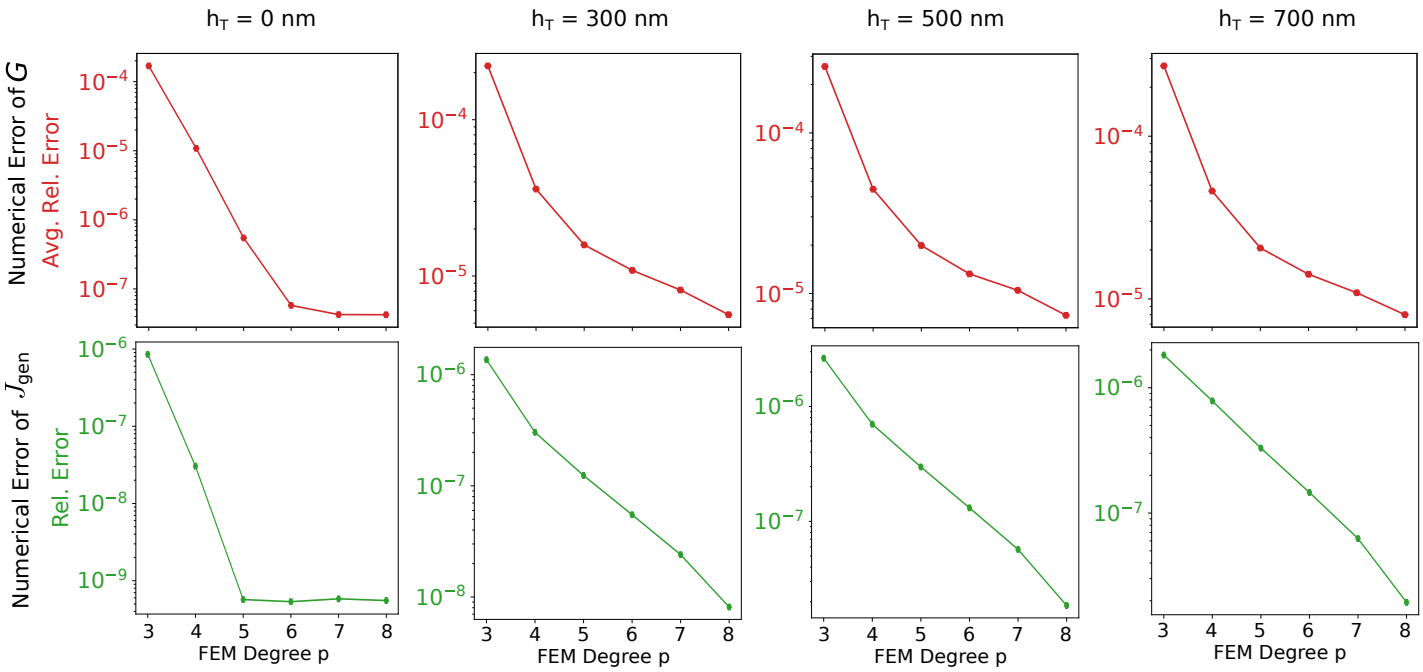

FIG. S14. The numerical error of the finite element simulation with respect to the used polynomial degree p and fixed maximum side length $h = 0.5$. (a) The average relative error of the photogeneration rate G. (b) The relative error of the generated current density J_{gen}.

mation quality on each finite element, which, in turn, reduces the numerical error. Similarly, decreasing the maximum element side length h leads to a finer mesh and allows for a more accurate representation of the geometry and solution. To quantify the error, we compute the relative error $\epsilon_{rel} := (u_k - u)/u$, where $k \in p, h$. Here, u_k denotes the numerical solution computed with a given polynomial degree p or mesh size h, and u is a reference solution obtained with high p or small h, respectively. Figure S14 shows the average relative error in the photogeneration rate $G(\mathbf{x})$ as well as the relative error of the generated current density J_{gen} in dependence of the polynomial degree p.

REFERENCES

[1]J. Pomplun, S. Burger, L. Zschiedrich, and F. Schmidt, Phys. Status Solidi B **244**, 3419 (2007), http://jcmwave.com.

[2]J.-M. Jin, *The Finite Element Method in Electromagnetics*, 3rd ed. (Wiley, New York, 2014).

[3]U.S. Department of Energy (DOE)/NREL/ALLIANCE, Reference Air Mass 1.5 Spectra, https://www.nrel.gov/grid/solar-resource/spectra-am1.5.html.

[4]P. Manley, dispersion, https://dispersion.readthedocs.io/en/latest/index.html.

[5]R. Santbergen, T. Meguro, T. Suezaki, G. Koizumi, K. Yamamoto, and M. Zeman, IEEE Journal of Photovoltaics **7**, 919 (2017).

[6]L. Mazzarella, M. Werth, K. Jäger, M. Jošt, L. Korte, S. Albrecht, R. Schlatmann, and B. Stannowski, Opt. Express **26**, A487 (2018).

[7]J. A. Guerra, A. Tejada, L. Korte, L. Kegelmann, J. A. Töfflinger, S. Albrecht, B. Rech, and R. Weingärtner, Journal of Applied Physics **121**, 173104 (2017).

[8]D. Menzel, A. Al-Ashouri, A. Tejada, I. Levine, J. A. Guerra, B. Rech, S. Albrecht, and L. Korte, Advanced Energy Materials **12**, 2201109 (2022).

[9]D. Abdel, C. Chainais-Hillairet, P. Farrell, and M. Herda, IMA Journal of Numerical Analysis **44**, 1090 (2024).

[10]D. Abdel, A. Glitzky, and M. Liero, Discrete and Continuous Dynamical Systems - B **30**, 99 (2024).

[11]D. Abdel, N. E. Courtier, and P. Farrell, Optical and Quantum Electronics **55**, 884 (2023).

[12]D. Abdel, P. Vágner, J. Fuhrmann, and P. Farrell, Electrochimica Acta **390**, 138696 (2021).

[13]D. Abdel, *Modeling and simulation of vacancy-assisted charge transport in innovative semiconductor devices*, PhD Thesis, Freie Universität Berlin (2024).

[14]V. M. Le Corre, J. Diekmann, F. Peña-Camargo, J. Thiesbrummel, N. Tokmoldin, E. Gutierrez-Partida, K. P. Peters, L. Perdigón-Toro, M. H. Futscher, F. Lang, J. Warby, H. J. Snaith, D. Neher, and M. Stolterfoht, Solar RRL **6**, 2100772 (2022).

[15]J. Diekmann, P. Caprioglio, M. H. Futscher, V. M. Le Corre, S. Reichert, F. Jaiser, M. Arvind, L. P. Toro, E. Gutierrez-Partida, F. Peña Camargo, C. Deibel, B. Ehrler, T. Unold, T. Kirchartz, D. Neher, and M. Stolterfoht, Solar RRL **5**, 2100219 (2021).

[16]W. Clarke, L. Bennett, Y. Grudeva, J. Foster, G. Richardson, and N. Courtier, Journal of Computational Electronics **22**, 364–382 (2022).

[17]P. Farrell, D. H. Doan, M. Kantner, J. Fuhrmann, T. Koprucki, and N. Rotundo, in *Handbook of Optoelectronic Device Modeling and Simulation: Lasers, Modulators, Photodetectors, Solar Cells, and Numerical Methods, Vol. 2* (CRC Press Taylor & Francis Group, 2017) pp. 733–771.

[18]J. Thiesbrummel, S. Shah, E. Gutierrez-Partida, F. Zu, F. Peña-Camargo, S. Zeiske, J. Diekmann,

F. Ye, K. P. Peters, K. O. Brinkmann, P. Caprioglio, A. Dasgupta, S. Seo, F. A. Adeleye, J. Warby, Q. Jeangros, F. Lang, S. Zhang, S. Albrecht, T. Riedl, A. Armin, D. Neher, N. Koch, Y. Wu, V. M. Le Corre, H. Snaith, and M. Stolterfoht, Nature Energy **9**, 664 (2024).

[19]M. Stolterfoht, C. Wolff, J. Marquez-Prieto, S. Zhang, C. Hages, D. Rothhardt, S. Albrecht, P. Burn, P. Meredith, T. Unold, and D. Neher, Nature Energy **3**, 847 (2018).